



**LUND**  
UNIVERSITY

**Master of Science Thesis**

# **Distortion in 3T clinical fMRI data**

**Peter Mannfolk**

**Supervisor: Johan Olsrud**

**Department of Radiation Physics  
Lund University, 2003**

**LUJI-RADFYS-EX-1/2003**

## Sammanfattning

Funktionell magnetresonanstomografi (fMRI) är en teknik som gör det möjligt att kartlägga aktivering inom olika delar av hjärnan. Genom att samla in bilddata då patienten är i vila, och sedan jämföra dessa med data insamlade medan patienten är aktiv (t.ex. utför fingerrörelser), kan en bild skapas som visar var i hjärnan aktivering har skett. Dessa bilder kan t.ex. användas för att bedöma om det är möjligt att operera bort en tumör utan att samtidigt skada viktiga funktionscentra i hjärnan.

För att kunna genomföra en funktionell studie krävs mycket snabba bildtagningssekvenser. Dessa ger dock bilder som på olika sätt innehåller störningar, vilket kan ge upphov till feltolkning av resultaten. Detta projekt har haft som mål att mäta storleken på störningar i funktionella studier, för att på så sätt kunna bedöma resultatens tillförlitlighet.

Ett datorprogram har skrivits, vilket förutom att analysera bilder med störningar även gör en korrektion av dessa.

# Contents

1	Introduction .....	1
1.1	Background .....	1
1.2	BOLD Functional MRI – an overview.....	1
1.2.1	Characteristics of the BOLD signal .....	1
1.2.2	Paradigm design .....	3
1.2.3	Analysis of the fMRI Data .....	3
1.2.4	Echo Planar Imaging .....	5
1.2.5	Artefacts .....	7
1.3	Measurement and correction of distortion .....	8
2	Theory .....	10
2.1	Magnetic field changes due to variations in susceptibility .....	10
2.2	The field map .....	13
2.3	Phase Unwrapping.....	14
2.4	The correction algorithm.....	15
2.5	Estimation of expected distortions .....	16
3	Materials and Methods .....	17
4	Results .....	19
5	Discussion .....	24
6	References .....	27
7	Appendix .....	29
7.1	The program .....	29

# 1 Introduction

## 1.1 Background

Functional MRI (fMRI) is a technique for determining which parts of the brain are activated when a subject experiences some type of physical sensation or performs an activity. This technique has during the past several years become a very useful tool for understanding functions of the nervous system, and the development of clinical applications is rapidly progressing. However, fMRI is not straightforward and attention must be paid to many details in the process. One necessity when performing an fMRI experiment is the use of very rapid imaging techniques. Images acquired with these techniques suffer from different types of artefacts such as geometric distortion, which could for example lead to misinterpretation of activation maps, or can be misleading when using fMRI for presurgical planning. The main objective of this work was to evaluate the effects of geometric distortion when performing fMRI experiments at the 3T dedicated head scanner (Siemens Magnetom Allegra) at Lund University Hospital. A correction method based on the evaluation technique was also implemented and applied to the distorted images.

The introduction to this report gives a brief background to the particular fMRI method used in this work (the so-called BOLD fMRI technique), as well as to rapid imaging (echo planar imaging) in order to define the problem. Also, an overview of related works is given.

## 1.2 BOLD Functional MRI – an overview

### 1.2.1 Characteristics of the BOLD signal

There are different approaches to fMRI, such as perfusion-based methods and flow-based methods. The method that has been used throughout this work utilizes the so-called BOLD contrast, i.e. blood oxygenation level dependent contrast, which was first demonstrated in human brain in 1992 [1-3]. This is a method that measures the effects of cerebral blood oxygenation caused by an increased activity in the human cortex, which in turn is caused by activity of some kind from the subject. In order to produce energy the brain needs oxygen to metabolise glucose. The oxygen needed in this process is supplied via the blood. The part of the blood that carries oxygen is the protein called haemoglobin – the red blood cells. When an oxygen molecule is bound to haemoglobin, it is called oxyhaemoglobin, otherwise it is called deoxyhaemoglobin. It is the magnetic properties of these two types of haemoglobin which gives rise to the contrast mechanism used in fMRI, known as the blood oxygen level dependent (BOLD) contrast.

There is a difference in magnetic properties between the two types of haemoglobin in that deoxyhaemoglobin is paramagnetic whereas oxyhaemoglobin is diamagnetic. The paramagnetic property of deoxyhaemoglobin causes a susceptibility difference between a blood vessel that contains deoxyhaemoglobin and the surrounding tissue. This causes more rapid dephasing of the transverse magnetization, i.e.  $T2^*$  is reduced. Since oxyhaemoglobin is

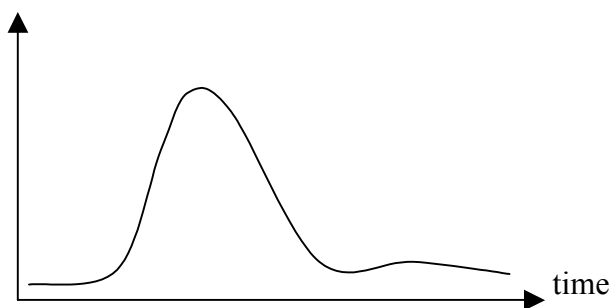
diamagnetic and therefore not causes any additional dephasing, the difference in oxygenation of the blood will manifest itself as signal changes in  $T2^*$  weighted ( $T2^*W$ ) images. Given that the level of oxygen consumption is increased upon neural activity, a decrease in the amount of oxyhaemoglobin and therefore a relative increase in the amount of deoxyhaemoglobin would result. This would cause a signal drop in  $T2^*W$  images. On the contrary, what is seen in practice is a signal increase, due to the fact that the amount of oxygen decrease is compensated by a much larger increase in cerebral blood flow. Thus, the amount of oxyhaemoglobin – and therefore also the signal –increases.

When studying brain function using BOLD fMRI not only the amount of signal change is of importance but also the time characteristics of the signal change. When the subject is repeatedly presented with a stimulus or carries out some task, e.g. finger tapping, this onsets neural activity.

The time between the neural activation and the onset of BOLD signal change is approximately 2 s. The signal then increases during 6-9 s, reaching a plateau. When the neural activity ceases, the signal eventually returns to the baseline. This takes 1-2 s longer than the initial increase. Fig. 1.1 shows an example of the BOLD response following stimulus presentation. There have also been observations of a signal dip before and after the period of increased BOLD signal [2,4]. The first dip is believed to be due to the initial draining of oxygen as a response to neural activity, resulting in a local increase in the amount of deoxyhaemoglobin. The haemodynamic response, i.e. the overcompensation of the decreased amount of oxyhaemoglobin eventually causes the signal to increase.

To explain the post-stimulus signal an assumption is made that the blood flow as well as the oxygen consumption decreases after the end of the stimulus. The blood volume and therefore also the amount of deoxyhaemoglobin however remains elevated, resulting in a signal dip. Other explanations have been proposed, e.g. the Balloon model [5], which also suggests that the blood volume effect is the reason for the signal dip.

BOLD response



Stimuli



Fig. 1.1. The BOLD response (top) following stimulus presentation (bottom).

## 1.2.2 Paradigm design

In order to make use of the BOLD response in various studies, an important part of fMRI is the design of the stimulus paradigm. A common experimental design is the blocked-trial paradigm in which sequences of stimuli are presented during relatively long periods (blocks) (fig. 1.2 (a)). For example, a block might consist of a sequence of words to be remembered. The summed BOLD response to the stimuli is then studied across the entire block.

Another common design, referred to as single trial or event-related paradigms attempts to isolate individual events (fig. 1.2 (b)). These techniques allow for greater flexibility in the experimental designs, as the BOLD response to different stimulus events can be selectively processed.

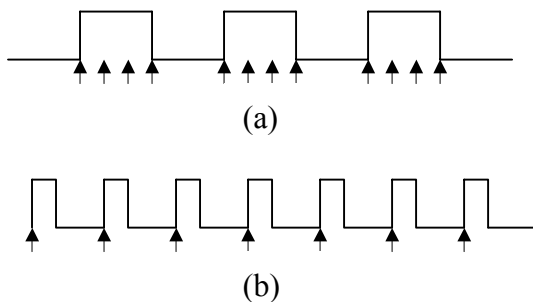


Fig. 1.2. The difference between blocked-trial and event-related paradigms. (a) A blocked-task paradigm with sequential presentation of many events of the same type as indicated by the closely spaced arrowheads. The average signal change across one entire block is then studied. (b) An event-related paradigm separates the individual events. This provides more options when designing experiments, as well as a means of studying the dynamics of the BOLD response.

## 1.2.3 Analysis of the fMRI Data

Since an fMRI experiment normally is performed using multiple imaging slices, after performing an experiment, one ends up with a large number of images. In order to correctly identify the activated areas, there may be several approaches. One obvious method to reveal signal changes is to subtract averaged images acquired during periods of stimulus presentation from averaged images acquired when the stimulus is not present. This however yields results that are very sensitive to subject movement. A more common approach is to use statistical methods such as the Student's t-test. This test compares the difference in means with the difference in standard deviation for periods when stimulus is turned on and off respectively. The resulting t-scores are high for pixels with large probability of activation (i.e. large differences in means with small standard deviations). The result will be a value assigned to each pixel, corresponding to the probability of the response in that specific location. The resulting images are called statistical parametric maps.

Another way of conducting the statistical testing is to predict the shape of the response to the stimulus. Correlation coefficients between a reference response function and the actual pixel activation over time are then calculated. With this technique, an appropriate reference response function is essential. A first approximation is to model the response as a square wave. This is however not a particularly good estimate of the smooth actual response

function. The square wave model is also sensitive to any delays in the response, an effect that can be compensated for by changing the phase of the square wave, i.e. setting a delay of typically 5 s.

More realistic models include using the average of known response functions to one type of stimulus as a prediction of the actual response. Yet another approach is to use a mathematical model of the response function, e.g. the Poisson function.

All these models can be described as special cases of the so-called General Linear Model, (GLM). This model fits the observed pixel values to a so-called design matrix that contains vectors (regressors) corresponding to the periods when stimulus is turned on and off, respectively. This can be expressed as:

$$Y = X\beta + \varepsilon \quad (1.1)$$

, where  $Y$  is the matrix containing the pixel values,  $X$  is the design matrix,  $\beta$  is a vector containing coefficients corresponding to the “best” fit, and  $\varepsilon$  is the error matrix. The assumed model of the stimulus response  $\beta$ , can then be statistically tested for significance by examining the error matrix,  $\varepsilon$ . The GLM provides a framework that also allows for modelling of confounding factors such as respiration, provided that the time course of these factors can be modelled.

Finally, to display the localisation of activated areas, statistical maps are generally co-registered with anatomical images. Since functional imaging requires very rapid scanning techniques yielding images with relatively low spatial resolution, co-registration is often done with high-resolution images as shown in Fig. 1.3.

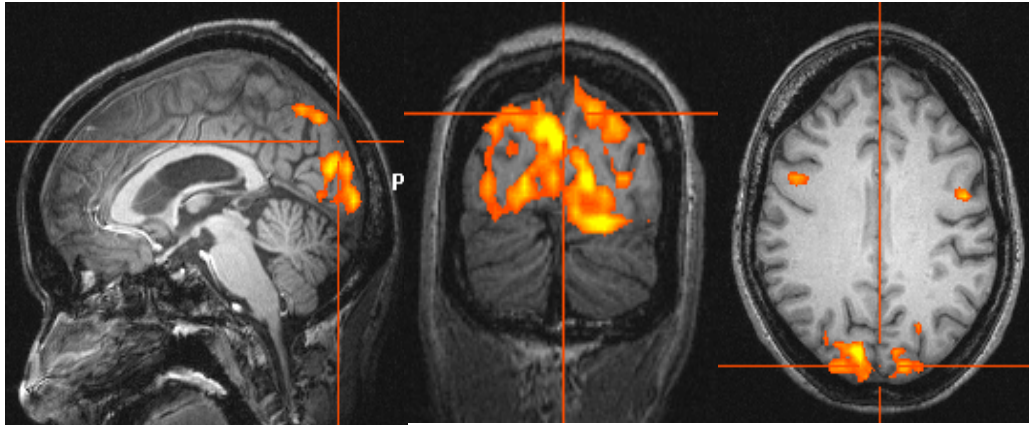


Fig. 1.3. From left to right: Sagittal, coronal and transverse views of the results of an fMRI experiment with visual cortex stimulation. The maps of statistically determined “active” pixels are co-registered with a high-resolution anatomical image, and displayed using a colour-scale showing the degree of significance.

## 1.2.4 Echo Planar Imaging

In order to study brain function using fMRI, very rapid imaging is required to obtain sufficient amounts of time-resolved data for the statistical evaluation. A rapid imaging sequence also reduces artefacts from subject movements and has the advantage of rendering the BOLD response to short stimuli. A suitable sequence for fMRI that meets these requirements is the gradient echo – echo planar imaging sequence (GRE-EPI). It provides T2\* weighted images in order to show the BOLD contrast.

The difference between conventional MRI and echo planar imaging can be described in terms of k-space. The signal coordinates in k-space correspond to the time integral of the gradient amplitude in each direction:

$$k_i(t) = \gamma \cdot \int G_i(t) dt \quad (1.2)$$

where  $k_i$  is the location along the  $i$ -axis,  $G_i$  is the gradient amplitude as a function of time,  $\gamma$  is the Larmor constant, and  $t$  is the gradient duration. In conventional MRI, k-space is covered line by line, with a new RF excitation for each k-space line. This means that the total acquisition time depends on the time between excitations, TR, and the number of k-space lines collected (number of phase encoding steps).

In EPI all data are collected after only one RF excitation. This is performed using an oscillating readout gradient. Following each readout line, a so-called phase blip, i.e. a short pulse of the phase encoding gradient, gives the k-space trajectory its meandering characteristic (figs. 1.4 and 1.5). Since T2 for human brain tissue is approximately 100 ms, and T2\* even shorter, the entire k-space has to be covered very rapidly when using EPI in order to avoid total signal decay. Therefore high amplitude gradients and rapid sampling are used with EPI. In conventional MRI bandwidths of about 30 kHz are used, while for EPI corresponding values are about 300 kHz.

This introduces some drawbacks to EPI imaging. The use of high bandwidths cause an SNR drop relative to conventional imaging. Also, the fact that the required gradients cannot instantly reach the large magnitudes needed means that the rise time becomes a too significant fraction of the acquisition time, which limits the practically available image resolution. There is also an inevitable decay of the signal during image acquisition, which will introduce blurring to the images. The practical solution is to perform the EPI with low resolution, e.g. using 64 x 64 matrices.



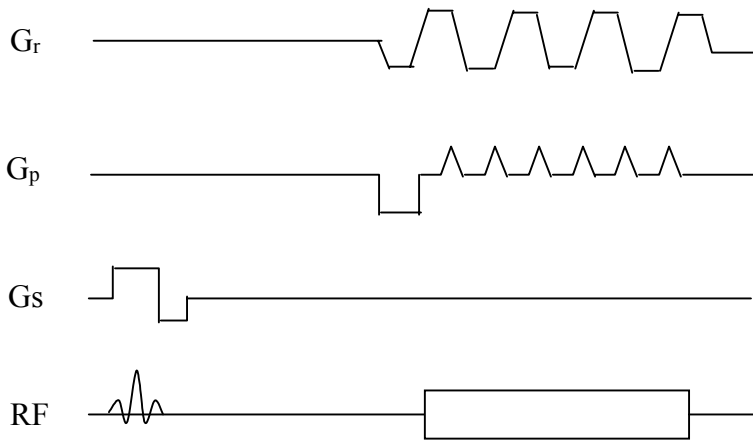


Fig. 1.4. Pulse sequence timing diagram for the blipped EPI sequence.

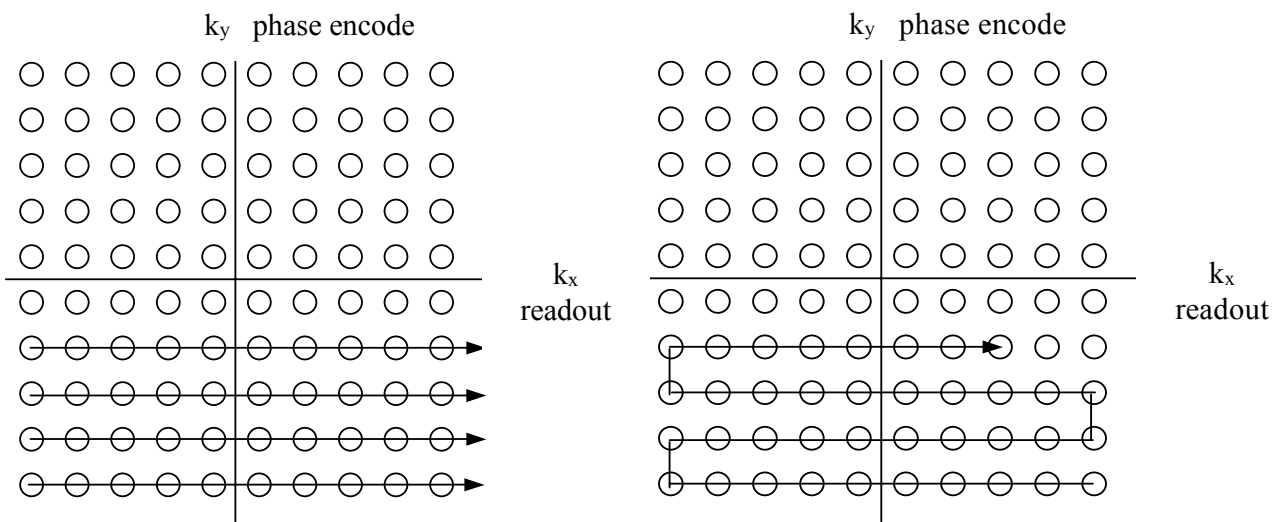


Fig. 1.5. The difference between k-space traversals for conventional (left) and blipped echo planar imaging (right).

### 1.2.5 Artefacts

In order to achieve a good geometrical accuracy between activation images acquired with EPI and high-resolution anatomical images, the EPI images cannot be distorted to any great extent. However, there are artefacts connected with EPI imaging which can lead to gross distortion and subsequent misinterpretation when evaluating the anatomical localisation of neural activation.

A crucial parameter when using EPI, is as described previously, the bandwidth. This is very high along the readout direction, but since adjacent points in the phase encoding direction are sampled at a much slower rate, the resulting bandwidth in this direction is typically 30 Hz/pixel. This makes EPI images sensitive to off resonance effects in the phase encoding direction leading to several artefacts. One of these artefacts is the so-called chemical shift artefact. The electron distribution around protons in water compared to protons in fat is different, which means that the shielding from the static field, and therefore the resonance frequency, will depend on if a proton is in water or in fat. The result is that signal from tissues of different chemical properties is spatially shifted. In conventional MRI this shift only occurs in the readout direction, but for EPI, since all data is collected after one RF pulse the shift is also -and more severely - present in the phase encoding direction. In EPI images acquired with a 3T scanner the fat water chemical shift can be as large as 5 cm. On most modern scanners there are, however, correction methods for the chemical shift, which significantly reduces these artefacts.

Another artefact is known as “N/2 ghosting”, and is a result of the large eddy currents induced when using EPI. These eddy currents are induced in various electrically conductive parts of the scanner when the gradients are switched on and off. The magnetic field gradients that are created by the eddy currents results in a frequency shift which, owing to the oscillating k-space trajectory manifests themselves as phase differences from line to line. After Fourier transformation the resulting image has parts of the signal shifted one half image in the phase encoding direction.

A third artefact is the geometric distortion caused by magnetic field inhomogeneity. This is due to the fact that susceptibility differences between different types of tissue results in slight disturbances of the main magnetic field. This occurs mainly in the vicinity of the interfaces between tissue and air or bone e.g. at the frontal and temporal lobes. A derivation of the magnetic field shift due to susceptibility differences is given in chapter 2.1. As mentioned above, due to the low bandwidth this results in a spatial signal shift of the signal in the phase encoding direction. In fMRI, this can lead to misinterpretation of activation maps, and furthermore, can be misleading when using fMRI for presurgical planning. The experimental part of this work is mainly focused on this type of artefact.

### **1.3 Measurement and correction of distortion**

Several different methods for measurement and correction of geometric distortion in EPI imaging have been proposed. One common approach, which is also adopted in this work, is the so-called field map method. This technique tries to map the magnetic field and thereafter, using this data, correct the distorted EPI images. A field map can be obtained after acquisition of two gradient-echo images (GRE) with different echo-times [6]. By subtracting the phase information in the two images from each other, differences that are equal in the two images can be eliminated and the resulting data together with the known echo-time difference therefore depicts the phase change due to field inhomogeneity. The resulting “phase map” can be scaled to represent the field inhomogeneity as a “field map”. This field map can in turn be scaled in order to obtain a so-called pixel displacement map that depicts how much each pixel has been shifted due to the field inhomogeneity. Hutton et al. [7] have a differing approach in that they have used two EPI acquired images instead of GRE images. The scaled pixel shift map is then used to sample the distorted EPI images in order to obtain undistorted images, which are finally intensity adjusted to account for the altering of voxel brightness that also is an effect of the geometrical distortion.

The same correction method is used by Schmithorst et al. [8], but using a so-called multiecho reference scan which is a modified EPI sequence. This reference scan is used to correct EPI images from different kinds of artefacts that occur, e.g. ghosting and geometrical distortion. In order to correct the particular case of geometrical distortion, the reference scan data is reordered to simulate the EPI images that are used to make the pixel shift maps.

Also Reber et al. [9] has used a field map based on EPI images. The pixel shift maps are then in a similar way as in the work of Hutton et al. used to resample the distorted images and thereby acquiring undistorted images. A way of making the computations less time consuming is proposed by Akel et al. [10]. Here EPI images are also used to calculate the field map, after first making the assumption that the additional phase introduced by the field inhomogeneity is linearly dependent of the k-space trajectory. They then use a linear estimation of the time map, i.e. the time at which each k-space value is acquired which for the trajectory of EPI sequences is a good estimation. The estimated time map can then be used together with the field map to calculate the actual off-resonance values.

The field map correction technique has a few disadvantages such as difficulties in calculating phase maps in regions with high field inhomogeneity due to loss of signal, and the problem of phase wrapping. The phase unwrapping can be quite complex to perform in practice, and will be discussed in more detail in chapter 2.2.

Another proposed correction technique uses the point spread function. The point spread function is a property of any imaging system and describes the magnitude and nature of spatial distortions. One can think of the point spread function as the description of how an imaging system blurs an ideal point shaped input impulse. The distortion information is reflected in the PSF and it can be shown that the measured image is the convolution of the PSF with the undistorted image. To obtain the undistorted image, a deconvolution of the measured image with the PSF is performed.

Robson et al. [11] have performed the measurement of the PSF by applying gradient pulses before the imaging. The gradients were applied in each of the two in-plane encoding directions. Fourier transformation was then performed with respect to the pre-imaging gradients and the imaging gradients, respectively. This yields the PSF in each pixel, which then can be used in a deconvolution process to obtain the undistorted EPI images. Since in EPI the dominant distortion is in the phase encoding direction, as discussed previously in ch.

1.2.5, only gradients in this direction have to be used, thereby shortening the scanning time. This have been done by Zeng and Constable [12] in their comparison between the field map method and the PSF method.

Although the two approaches discussed above may be considered to be two main branches among correction techniques, there are several other methods. Chen and Wyrwicz [13] are performing the correction in fourier space, applying a phase modulating factor which is unique for each line in the phase encoding direction. The phase modulating factor for each line is calculated from two gradient-echo images with the echo time difference equal to the phase accumulation time for that particular line. This avoids the complex problem of phase unwrapping that accompanies the field maps. Also Kadah and Hu [14] have performed the correction in k-space by use of an initially acquired field map as a template for the correction. Instead of using two images obtained with different echo times as a field map, Luk-Pat and Nishimura [15] proposes interpolation between two EPI images in order to acquire an image that corresponds to acquiring all of the data at a constant time after the RF pulse.

## 2 Theory

### 2.1 Magnetic field changes due to variations in susceptibility

As previously described, echo planar imaging suffers from geometric distortion mainly in the phase encoding direction, due to phase changes caused by susceptibility effects. Moving from one region to another, the magnetic field changes due to variations in susceptibility. This in turn results in a phase change at the acquisition (echo) time ( $T_E$ ) given by:

$$\Delta\phi = -2\pi \cdot \gamma \cdot \Delta B \cdot T_E \quad (2.1)$$

, where  $\gamma$  is the gyromagnetic ratio and  $\Delta B$  is the magnetic field change. The field change due to the susceptibility differences between tissues can be illustrated by considering a sphere of radius  $a$ , and with constant susceptibility  $\chi$  in a uniform static magnetic field  $\vec{B}_0 = B_0 \hat{z}$  in the  $z$ -direction, where  $\hat{z}$  is the unity vector. The field outside the sphere at a position  $\vec{r}$  can be described as having one constant field contribution, and one dipole field contribution:

$$\vec{B}_{\text{out}}(\vec{r}) = B_0 \hat{z} + \frac{\mu_0}{4\pi} \frac{3(\vec{\mu}_m \cdot \hat{r})\hat{r} - \vec{\mu}_m}{r^3} \quad (2.2)$$

where  $\mu_0$  is the permeability in free space,  $\hat{r}$  is the unity vector, and the magnetic dipole moment is:

$$\vec{\mu}_m = \frac{4\pi}{3} a^3 M(\chi) \hat{z} \quad (2.3)$$

with the magnetization  $M(\chi)$ .

Inside the sphere, the magnetic field can be described as:

$$\vec{B}_{\text{in}} = B_{\text{in}} \hat{z} = \frac{1+\chi}{\chi} \mu_0 M(\chi) \hat{z} \quad (2.4)$$

The boundary conditions to be satisfied are the continuity of the field across the surface of the sphere, that  $\vec{B}_{\text{out}}$  equals  $B_0$  far from the sphere, and that the field is finite at the origin, i.e., at the centre of the sphere. These conditions are fulfilled by a constant magnetization vector inside the sphere:

$$\vec{M}(\chi) = \frac{3\chi}{3+\chi} \frac{\vec{B}_0}{\mu_0} \quad (2.5)$$

Combination of (2.2), (2.3) and (2.5) yields:

$$\vec{B}_{\text{out}} = B_0 \left( \hat{z} + \frac{\chi}{3+\chi} \left( \frac{a}{r} \right)^3 (3\hat{r}^2 \hat{z} - \hat{z}) \right) \quad (2.6)$$

With polar angle  $\theta$  as defined in fig.2.1 and from the definition of the scalar product,

$$\hat{\mathbf{r}} \cdot \hat{\mathbf{z}} = |\hat{\mathbf{r}}| \cdot |\hat{\mathbf{z}}| \cdot \cos \theta \quad (2.7)$$

this yields:

$$\bar{\mathbf{B}}_{\text{out}} = \mathbf{B}_0 \left( \hat{\mathbf{z}} + \frac{\chi}{3+\chi} \left( \frac{a}{r} \right)^3 (3 \cos \theta \hat{\mathbf{r}} - \hat{\mathbf{z}}) \right) \quad (2.8)$$

Combining (2.4) and (2.5) gives the field inside the sphere:

$$\bar{\mathbf{B}}_{\text{in}} = 3 \mathbf{B}_0 \frac{1+\chi}{3+\chi} \hat{\mathbf{z}} \quad (2.9)$$

The change of the field outside the sphere is:

$$\Delta \bar{\mathbf{B}}_{\text{out}} = \mathbf{B}_0 \left( \hat{\mathbf{z}} + \frac{\chi}{3+\chi} \left( \frac{a}{r} \right)^3 (3 \cos \theta \hat{\mathbf{r}} - \hat{\mathbf{z}}) \right) - \mathbf{B}_0 \hat{\mathbf{z}} \quad (2.10)$$

$$= \mathbf{B}_0 \frac{\chi}{3+\chi} \left( \frac{a}{r} \right)^3 \left( \frac{3 \cos^2 \theta}{\hat{\mathbf{z}}} - \hat{\mathbf{z}} \right) \quad (2.11)$$

, and the change in the z component due to the presence of the sphere is:

$$\Delta B_{\text{out}} \hat{\mathbf{z}} = \mathbf{B}_0 \frac{\chi}{3+\chi} \left( \frac{a}{r} \right)^3 (3 \cos^2 \theta - \hat{\mathbf{z}}^2) \quad (2.12)$$

$$\Delta B_{z,\text{out}} = \mathbf{B}_0 \frac{\chi}{3+\chi} \left( \frac{a}{r} \right)^3 (3 \cos^2 \theta - 1) \quad (2.13)$$

For the field inside the sphere the change is:

$$\Delta \bar{\mathbf{B}}_{\text{in}} = 3 \mathbf{B}_0 \frac{1+\chi}{3+\chi} \hat{\mathbf{z}} - \mathbf{B}_0 \hat{\mathbf{z}} \quad (2.14)$$

$$= \mathbf{B}_0 \hat{\mathbf{z}} \left( \frac{2\chi}{3+\chi} \right) \quad (2.15)$$

which gives the z component:

$$\Delta B_{z,\text{in}} = \mathbf{B}_0 \left( \frac{2\chi}{3+\chi} \right) \quad (2.16)$$

Now the phase shift can be determined from (2.13) and (2.16) respectively, together with (2.1). This gives the shift due to external field changes governed by the change in susceptibility between the outside and the inside of the sphere.

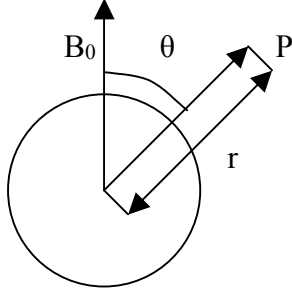


Fig. 2.1. Description of the field at a point P outside a magnetized sphere.

We have to this point assumed sharp interfaces between continuous media. However, neighbouring spins cannot be considered a continuous distribution of magnetic field sources. Due to a cancellation of the fields of nearby molecules, a correction has to be made to the susceptibility induced field changes. This so-called Lorentz correction gives for the special case of field changes inside and outside a sphere:

$$\Delta B_{z,\text{out}} = \frac{\Delta\chi}{3} \left(\frac{a}{r}\right)^3 (3\cos^2\theta - 1)B_0 + \frac{1}{3}\chi_e B_0 \quad (2.17)$$

$$\Delta B_{z,\text{in}} = \frac{1}{3}\chi_e B_0 \quad (2.18)$$

where  $\chi_i$  and  $\chi_e$  represents the susceptibility inside and outside the sphere, and  $\Delta\chi \equiv \chi_i - \chi_e$  (fig. 2.2). These corrections are only valid for small susceptibility values ( $\chi_i, \chi_e \ll 1$ ).

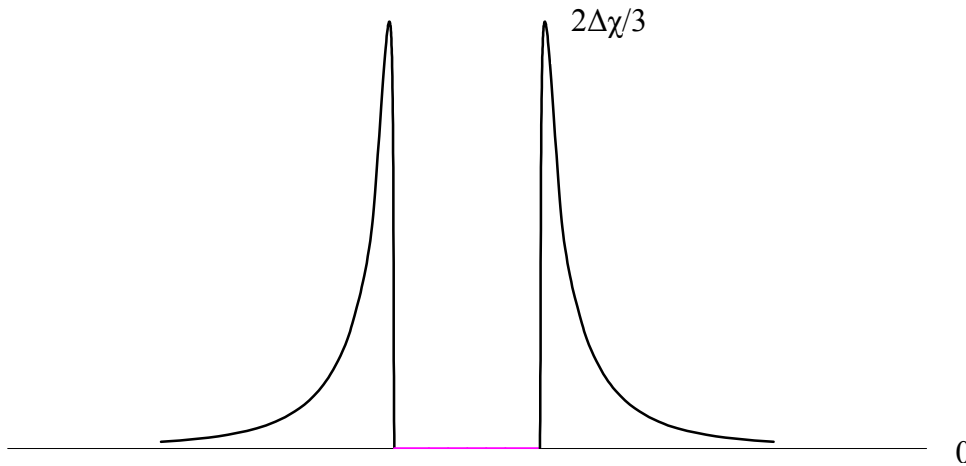


Fig. 2.2. Profile of the magnetic field shift due to the introduction of a spherical body in a medium with  $\chi_e = 0$ . Shifts are in units of  $B_0$  for a line along the diameter of the sphere and parallel to  $\vec{B}_0$ .

## 2.2 The field map

To generate a map of the signal displacements, it is necessary to collect a map of the field inhomogeneity  $\Delta B(x,y,z)$ , i.e., a field map. This is done as in the method of Jezzard and Balaban. Using eq.(2.1) this map can be calculated as:

$$\Delta B(x, y, z) = (2\pi \cdot \gamma \cdot T_E)^{-1} \Delta\phi(x, y, z) \quad (2.19)$$

Phase information can be obtained from the complex data of an MR image. This potentially yields the phase evolution information over the time  $T_E$ . To reflect  $\Delta B$ , two images with different echo times can be collected. The phase information is then extracted from the difference of the two phase images, which eliminates phase errors that are equal in the two images. Using this technique eq.(2.19) can be written as:

$$\Delta B(x, y, z) = (2\pi \cdot \gamma \cdot \Delta T_E)^{-1} \Delta\phi(x, y, z) \quad (2.20)$$

where  $\Delta T_E$  is the echo time difference between the two images and  $\Delta\phi(x,y,z)$  is the phase difference. When this scaling of the phase map to represent the field inhomogeneity is done, a conversion can be made into a map of spatial shifts in the phase encoding direction. This is achieved by multiplying the field map with the acquisition time:

$$d_y(x, y, z) = \gamma \Delta B(x, y, z) T_{acq} \quad (2.21)$$

where  $T_{acq}$  is the readout time for one image and  $d_y$  is the map of spatial shifts along the phase encoding direction (normally denoted the y direction, hence the subscript y). The shift map now represents how each voxel with coordinates  $(x,y,z)$  in the measured image has been shifted by  $d_y(x,y,z)$  due to  $\Delta B$ .

Since the evaluation of geometric distortion involves scaling of the field map in order to obtain the shift map, noise in the field map will introduce errors. It is therefore important to minimize the noise, which can be achieved by optimising the acquisition parameters. The echo time difference between the phase images could be increased in order to increase the signal-to-noise ratio in the calculated field maps. Another way of decreasing the noise is to perform spatial smoothing of the calculated field maps. Smoothing is effective in areas of the field map where the field varies slowly, but can introduce artefacts in areas where the field changes more rapidly.



## 2.3 Phase Unwrapping

One problem that arises when using phase information from field maps is that the measured phase difference is only uniquely defined in the interval  $[-\pi, \pi]$ . The actual phase difference however can take on any value, causing so-called wraps in measured field maps. The wraps manifest themselves as spatial discontinuities corresponding to offsets from the actual phase by integer multiples of  $2\pi$ :

$$\theta = \phi + 2\pi \cdot M \quad (2.22)$$

where  $\theta$  and  $\phi$  is the actual unwrapped and the wrapped phase difference respectively, and  $M$  is the integer offset. In order to acquire correct information from the field map, unwrapping of the field map has to be done, i.e. adding or subtracting multiples of  $2\pi$  to pixels where the phase difference is outside  $[-\pi, \pi]$ .

To address this problem, the algorithm as proposed by Jenkinson [16] have been used. The field map has been divided into  $N$  regions, each of which contains no phase wraps. The initial regions are constructed by dividing the phase interval  $[-\pi, \pi]$  into a number of subintervals. The field map is then split into connected regions, inside which the phase remains within a certain subinterval. These regions are then assigned unique numbers. In order to calculate the difference between two neighbouring regions, A and B, the sum of squared differences is used:

$$\begin{aligned} C_{AB} &= \sum_{j,k \in N(j)} (\theta_{Aj} - \theta_{Bj})^2 \\ &= \sum_{j,k \in N(j)} (\phi_{Aj} - \phi_{Bk} + 2\pi \cdot M_{AB})^2 \end{aligned} \quad (2.23)$$

where  $j$  and  $k$  are the indices of pixels belonging to the regions A and B, respectively. The indices  $j$  and  $k$  applies only to pixels which are neighbours.  $M_{AB}$  is the difference between the integer offsets applied to region A and B:

$$M_{AB} = M_A - M_B \quad (2.24)$$

To find the minimum of  $C_{AB}$ , differentiating with respect to  $M_A$  gives:

$$\frac{\partial C_{AB}}{\partial M_A} = 8\pi^2 N_{AB} M_{AB} + 4\pi P_{AB} = 0 \quad (2.25)$$

where  $N_{AB}$  is the number of neighbouring pixel pairs and  $P_{AB} = \sum_{j,k \in N(j)} (\phi_{Aj} - \phi_{Bk})$

Solving eq.(2.25) for  $M_{AB}$  yields:

$$M_{AB} = M_A - M_B = \frac{-P_{AB}}{2\pi N_{AB}} \quad (2.26)$$

Since this is an integer problem, the approach taken here is to compare the result of eq.(2.26) with the rounded result of the same equation, i.e:

$$K_{AB} = \text{round}(M_{AB}) \quad (2.27)$$

This leads to a cost difference:

$$\Delta C_{AB} = 8\pi^2 N_{AB} \left( \frac{1}{2} - |K_{AB} - M_{AB}| \right) \quad (2.28)$$

Calculating the differences for every neighbouring region pair and then selecting the regions where the difference is largest gives us the interface where an offset error would yield the worst results.

When a region pair is selected, these are merged into one new region using the rounded value  $K_{AB}$  as offset. Then the whole process is repeated until all regions have been merged into one single region.

## 2.4 The correction algorithm

In order to correct the distorted image, the unwrapping algorithm is applied to the phase difference images as described in the previous section. As in eq.(2.21) a scaling is then performed to the unwrapped images. This yields the shift maps that are used as templates in the correction process. The relationship between a pixel location in the distorted ( $y^{\text{distorted}}$ ) and a pixel location in the corrected image ( $y^{\text{corrected}}$ ) is given by:

$$y^{\text{distorted}} - d_y(y^{\text{corrected}}) = y^{\text{corrected}} \quad (2.29)$$

where  $d_y(y^{\text{corrected}})$  is the displacement of a pixel at location  $y^{\text{corrected}}$  as obtained from the shift map. Since the geometric distortion in the read direction has been ignored, the correction only applies to the phase encoding direction. Therefore, for each line in the echo planar image to be corrected, an interpolation of the signal intensity in the distorted image at location  $y^{\text{distorted}} - d_y(y^{\text{corrected}})$  is made and then placed at location  $y^{\text{corrected}}$  [6]. In the program that has been used in this work, the corrected image is reconstructed using an empty matrix where the interpolated intensities are placed at their respective locations ( $y^{\text{corrected}}$ ).

The interpolation method uses a sinc interpolation algorithm as in the work of Schmithorst et al. This algorithm performs interpolation by centering a sinc function on each sample. Each sinc function is scaled to match the value of the sample, and the frequency of the sinc functions is set to match the sample rate so that all neighbouring samples occur where the sinc functions have zero-crossings. All the sinc functions are then added together to form the interpolation.

## 2.5 Estimation of expected distortions

In order to get a first estimation of how severe the distortion problems are with the EPI fMRI scan protocol on the Siemens Magnetom Allegra scanner, a calculation can be made using the actual imaging parameters. According to Schmithorst, typical magnetic field inhomogeneity in the nasal sinuses is in the order of 1 ppm. Using the Larmor equation this corresponds to a frequency:

$$\Delta\nu = \gamma \cdot \Delta B = 42.6 \cdot 10^6 \cdot \frac{3}{10^6} = 128 \text{ Hz}$$

The EPI sequence used in the standard fMRI protocol at Lund University Hospital has an echo spacing of 0.44 ms. Using a 64x64 matrix, this yields the total acquisition time:

$$T = 64 \cdot 0.44 \text{ ms} = 28.2 \text{ ms}$$

According to the Fourier shift theorem, the bandwidth per pixel is obtained by taking the reciprocal of the total acquisition time, i.e.:

$$\frac{\Delta f}{\text{pixel}} = \frac{1}{T} = \frac{1}{28.2 \text{ ms}} = 35.5 \text{ Hz/pixel}$$

The bandwidth per pixel combined with the frequency corresponding to a field inhomogeneity of 1ppm gives the displacement in pixels as:

$$\frac{\Delta\nu}{\Delta f / \text{pixel}} = \frac{128}{35.5} \approx 3.6 \text{ pixels}$$

A field of view equal to 192x192 mm<sup>2</sup> is used in the fMRI protocol, corresponding to a pixel size of 192/64 = 3 mm. This results in a displacement of:

$$\Delta r = 3.6 \cdot 3 = 10.8 \text{ mm}$$

Thus, given the estimated inhomogeneity of 1ppm we can assume a displacement of approximately 1 cm close to the nasal sinuses and less in more homogeneous regions of the brain.

### 3 Materials and Methods

Algorithms for scaling, unwrapping, distortion correction and assessment of distortion as described in the previous chapter were implemented in a program written in Interactive Data Language, IDL (Research Systems Inc.). All images were acquired on a 3T head scanner (Siemens Magnetom Allegra).

In order to calculate the pixel shift maps, a field map corresponding to each image slice in the fMRI study was acquired. The field maps were obtained using a gradient echo sequence pre-designed by the manufacturer. The gradient echo sequence provided phase difference maps by using two phase images that were subtracted from each other. The echo times for the two gradient echo images were 4.9 and 7.4 ms, respectively. These parameters were preset by the manufacturer in order to suppress the influence of off-resonance fat signals.

The functional data were acquired using a single shot EPI sequence with matrix size = 64x64, voxel size = 3x3x3 mm<sup>3</sup>, FOV = 192 mm x 192 mm, TE = 30 ms, TR = 3000 ms. Before scaling the phase maps into pixel shift maps, phase unwrapping was performed, using the region-merging algorithm described in chapter 2.2. The pixel shift maps obtained after the unwrapping procedure were then scaled to represent the displacements in mm. The functional EPI images were corrected using the interpolation algorithm described in chapter 2.4.

In order to emphasize the distortions and to clearly illustrate and coarsely validate the correction algorithm, EPI images of a spherical phantom were acquired, with a linear shim component in one direction (y-y) deliberately off-set. The possible influence of noise in the field maps was studied by assessing geometrical distortion using smoothed field maps. The smoothing was accomplished using a boxcar average (kernel size of 3x3 pixels). An estimate of the variations due to noise was obtained by applying 5 square regions of interest (5x5 pixels) to homogeneous areas of a field map slice.

For the assessment of geometrical distortion with the present fMRI protocol, 3 healthy volunteers and 6 patients with brain tumours (1 prior to and 5 after surgery) were studied. The fMRI studies included motor (fingertapping) and sensory (light rubbing of the palm) stimulation as well as word generation tasks.

The distortion evaluation was performed by applying square regions of interest (10x10 pixels) at the locations representing the primary sensorimotor cortex and Broca's area (fig. 3.1). This was done for the left and right hemisphere respectively. In the patient images, ROI:s were also placed in the proximity of, and in areas contralateral to, the tumour/resection area.

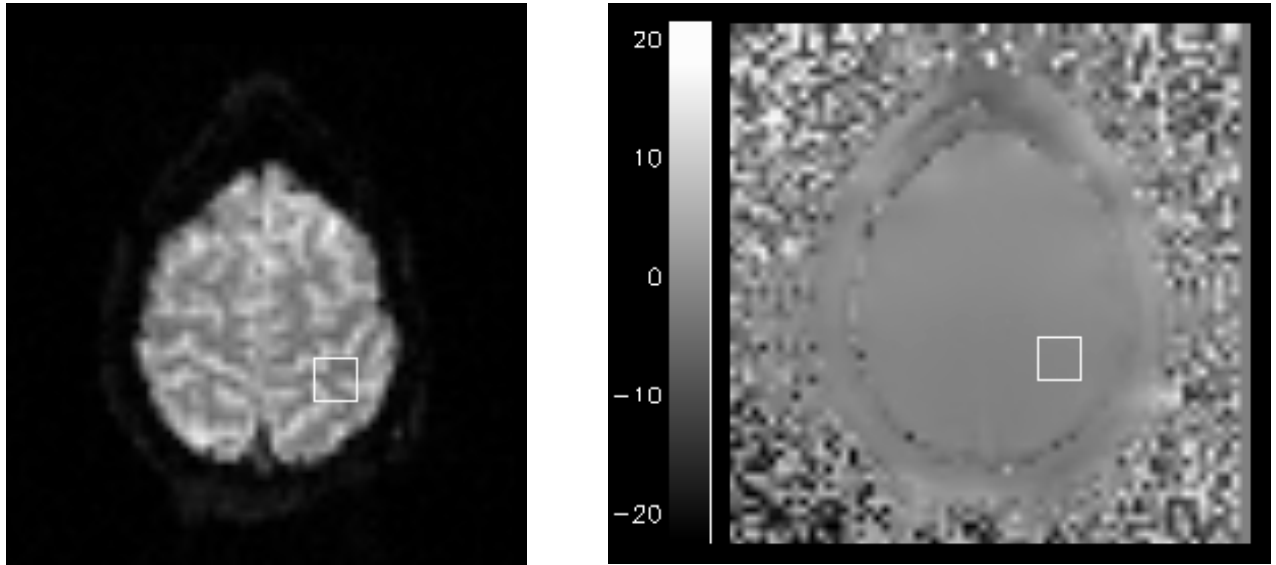


Fig. 3.1. Example images of the evaluation of spatial distortion. The left image shows the original EPI image with a ROI applied. The right image shows the corresponding shift map with a ROI automatically placed at the same location as in the EPI image. The greyscale bar shows the displacement in mm.

## 4 Results

The geometric distortion correction is shown in figure 4.1, where an EPI image of a cylindrical phantom was corrected. Here the y-y shim was deliberately off-set to emphasize the artefact and the correction method. The pixel shifts applied to the phantom image are shown in figure 4.2. Figure 4.3 shows an example image of a field map before and after applying the phase unwrapping algorithm. Example images of the noise evaluation are shown in figure 4.4 with the locations and numbering of the applied ROI:s. The statistics obtained from the ROI:s are presented in table 4.1. In figure 4.5 a pixel shift map of a healthy volunteer is shown together with the corresponding EPI image. The shift map is shown before and after smoothing with a boxcar average (kernel size of 3x3 pixels), and the EPI image is shown before and after correction, with the smoothed version of the field map as a template for the correction algorithm. Mean displacements for each ROI in sensorimotor cortex and in Broca's area for normal tissue are shown in figure 4.6 and 4.7 (3 healthy volunteers and 3 patients with tumour not located near the studied area). Figure 4.8 shows the mean displacement near the tumour/resection area and in the corresponding contralateral area in the same subject for 6 patients. Displacement was in most cases less than 3 mm in both primary sensorimotor cortex and in Broca's area, but varied more between subjects in Broca's area. Within subjects, displacement was similar when comparing both hemispheres, even for patients with titanium fixation clamps after surgery. All the examples are transversal images with the phase encoding direction in the vertical direction.

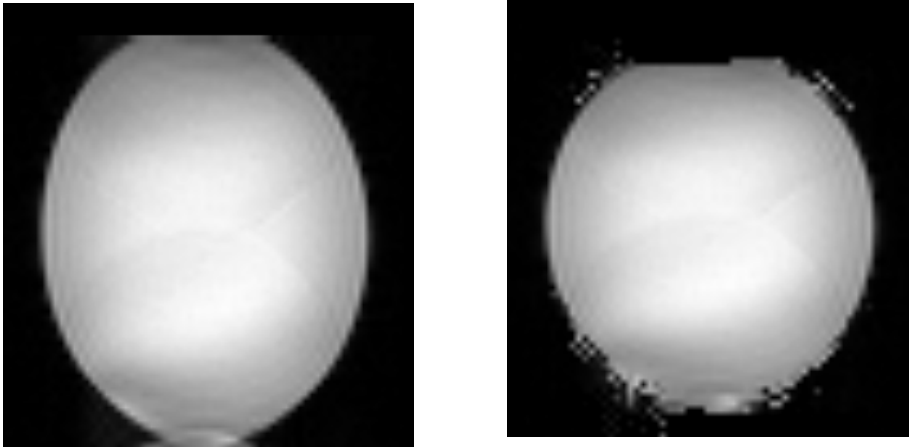


Fig. 4.1. Example images. EPI images of a spherical phantom before (left) and after (right) distortion correction using an unsmoothed shift map as correction template.

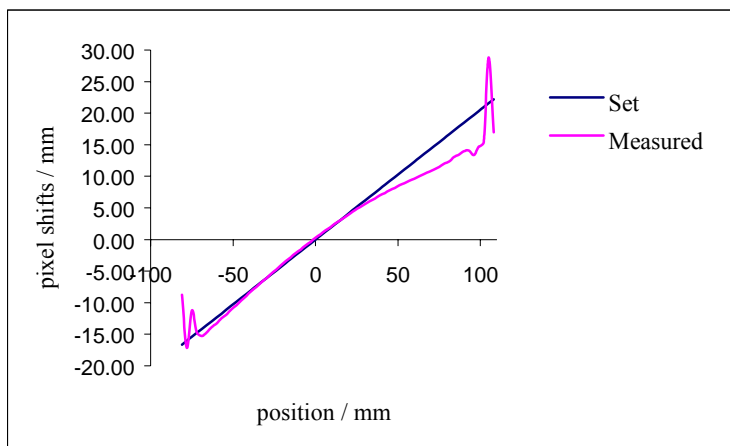


Fig 4.2. Pixel shifts applied to the distorted phantom image in fig. 4.1 as a function of position in the image (Negative values on the y-axis correspond to downward shifts, and negative values on the x-axis correspond to the upper part of the image). The shifts expected from the off-set shim are shown together with the shifts calculated from the actual field map.

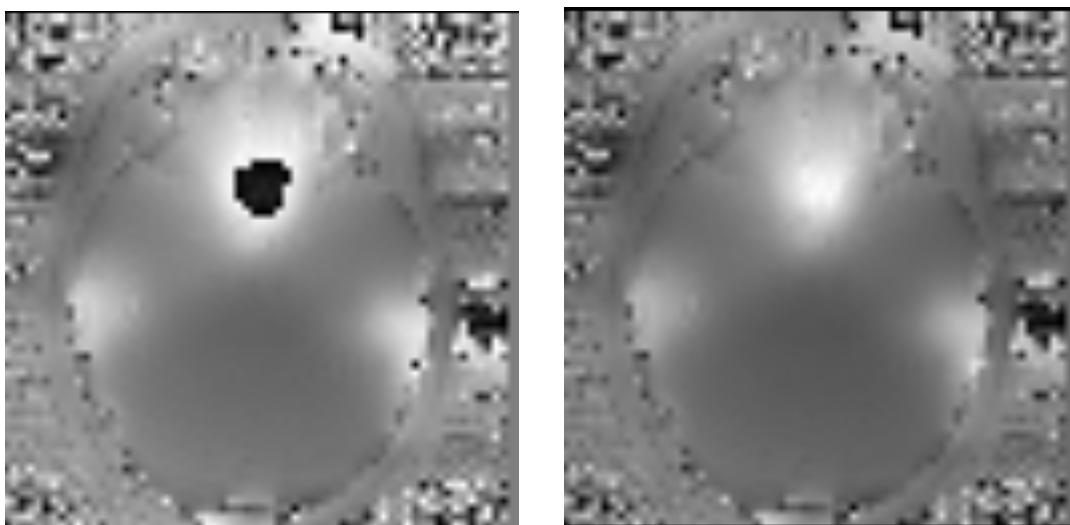


Fig. 4.3. Example images. Field maps before (left) and after (right) phase unwrapping.

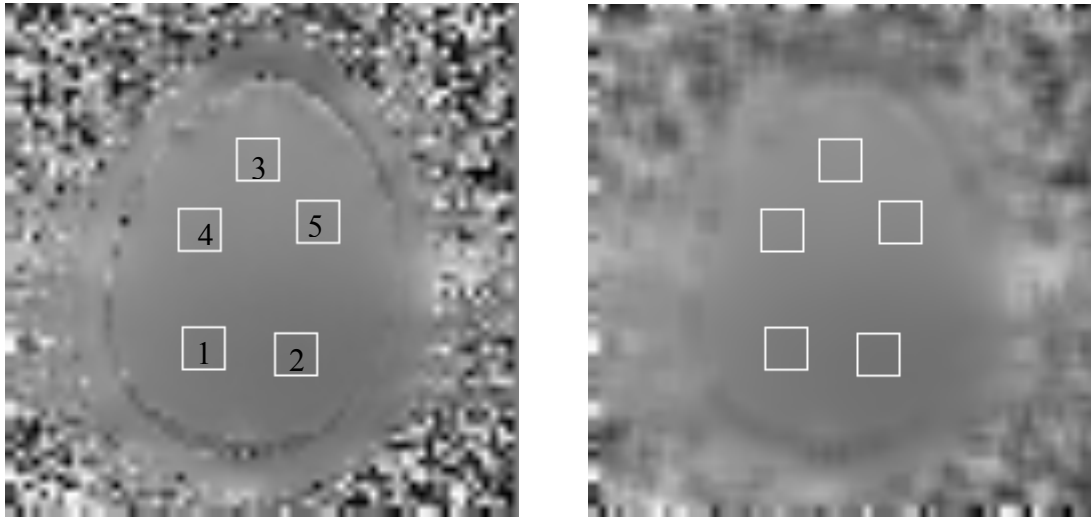


Fig. 4.4. The two shift maps that were used in the noise evaluation. The ROI:s where numbered and positioned according to the original (left) shift map. The same locations where used in the evaluation of the smoothed (right) shift map.

ROI no.	1	2	3	4	5
Original	0.17	0.15	0.17	0.22	0.22
Smoothed	0.17	0.13	0.15	0.21	0.20

Table 4.1. Standard deviations (in mm) for 5 ROI:s applied to a shift map and to a smoothed version of the same map as shown in figure 4.3.



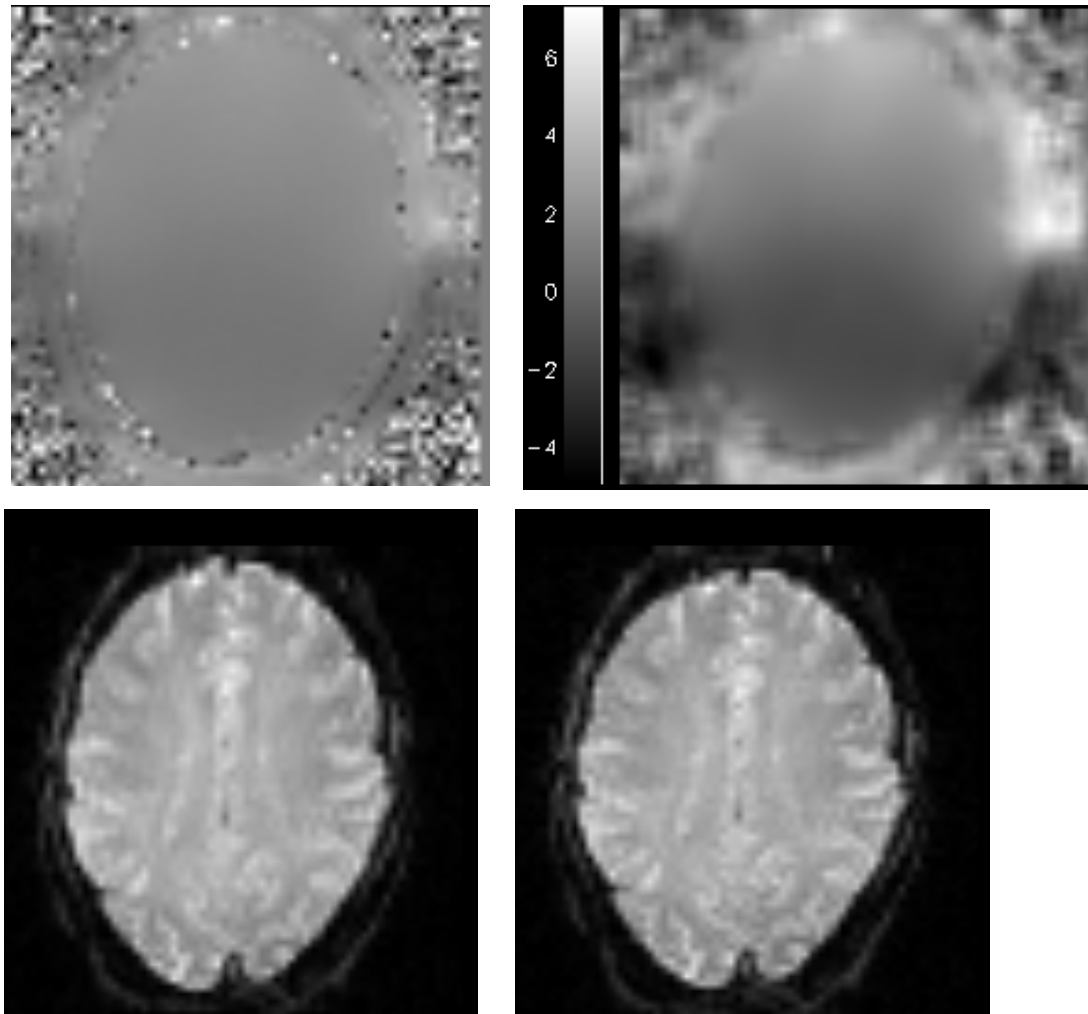


Fig. 4.5. Example images. The top left image shows a pixel shift map before smoothing. The top right image shows the smoothed version of the shift map together with a greyscale showing the displacements in mm. The bottom left image is the original EPI image to which the pixel shift map corresponds, and the bottom right image is the EPI image after applying the correction algorithm with the smoothed shift map as a template.

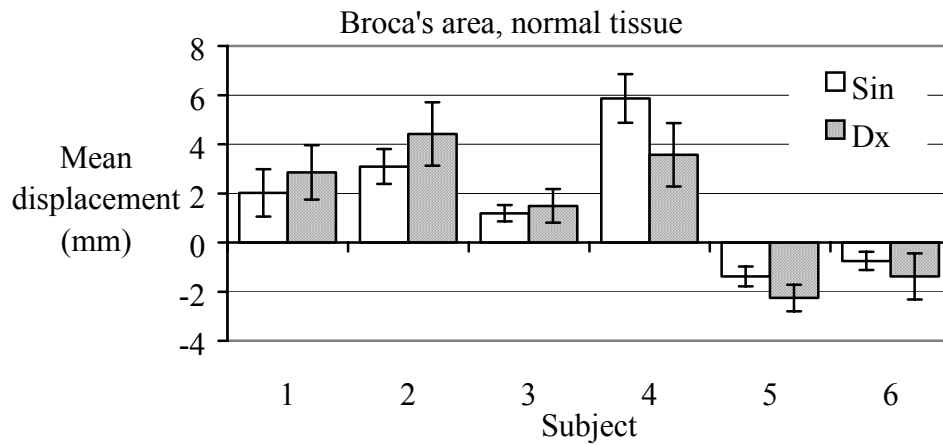


Fig. 4.6. Displacements (mean  $\pm$  1 SD) for each evaluated ROI (left and right side) in Broca's area.

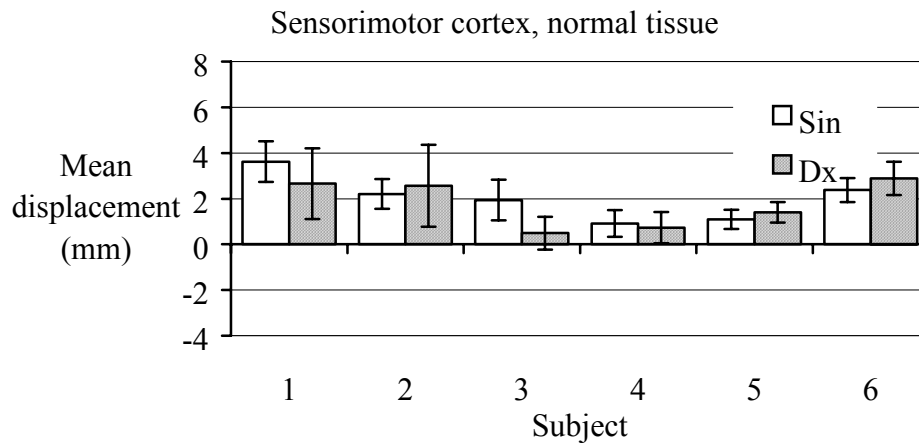


Fig. 4.7. Displacements (mean  $\pm$  1 SD) for each evaluated ROI (left and right side) in primary sensorimotor cortex.

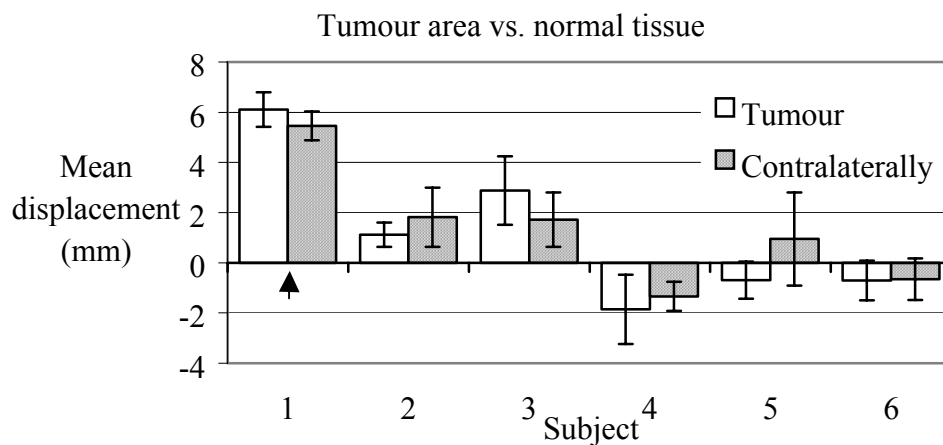


Fig. 4.8. Displacements (mean  $\pm$  1 SD) for each evaluated ROI in tumour/resection area and corresponding contralateral area. The arrow indicates the one subject that was examined prior to surgery.

## 5 Discussion

The evaluation of the geometrical distortion in patients and healthy volunteers showed that displacements are of low magnitude overall, both in primary sensorimotor cortex and in Broca's area. With a voxel size of  $3 \times 3 \times 3 \text{ mm}^3$ , the mean displacements were generally less than one voxel. Also, when evaluating the differences in displacement around tumour/resection areas compared to normal tissue contralaterally, no differences were found, which further supports co-registration of EPI images and anatomical images in the present fMRI studies. However, the larger intersubject displacement differences in Broca's area compared to those in the sensorimotor cortex reflect an increased influence of magnetic field inhomogeneity. This is probably due to the fact that Broca's area is located relatively close to the skull base where the proximity to air cavities can vary between the subjects. For subject 1 in fig. 4.7, the tumour was located frontally where the proximity to the frontal sinuses could also in this case explain the larger displacement.

The distortion correction algorithm implemented in this work appears to be effective when applied to the more superior slices of the brain. The phase wrapping artefacts were minimal in these regions of the brain, where there are no severe susceptibility artefacts. In the more inferior slices however, there are regions where the distortion is severe, and in some regions close to air cavities susceptibility differences have caused almost total signal loss. These areas can therefore not be properly corrected. Severe phase wrapping artefacts were also found in the more inferior parts of the brain. The region-merging algorithm managed to unwrap most of the slices, although noisy field maps makes this problem more difficult. Noise could not be altered by increasing the echo time difference since this was fixed in the GRE field map sequence. On the other hand, since the echo time difference was small (2.5 ms), the phase differences between the two images that were used to calculate the field map did generally not take on absolute values larger than  $\pi$ , which implies that few phase wraps were actually present. This trade-off between noise and phase artefacts might be further investigated and optimised, a task which however requires changing of the echo time differences. Another cause of artefacts in the corrected EPI images of the brain are partial volume effects arising from differences in precession frequency between fat and water in the same voxel. This can lead to erroneous phase measurements near tissue boundaries. However, by using boxcar average smoothing of the shift maps, these artefacts could be minimized.

When applied to an image of a spherical phantom, the correction algorithm also shows good results. However, random variation (noise) in the shift maps in turn generates artefacts in the corrected images, e.g. those shown in fig. 4.1 where artefacts are visible around the edges of the phantom. The effect of smoothing was to some extent reflected in the noise assessment. Although to a small extent, the smoothed shift maps showed somewhat decreased standard deviations in homogeneous areas (table 4.1). Smoothing of the field maps before the phase unwrapping or of the shift maps could be performed in different ways. In this work only a simple boxcar average was used. For further optimisation, a gaussian kernel might be used since this has been suggested to provide the best results (Hutton). It is also possible to generate a smoothed field map by fitting a smoothly varying function to it. This could be advantageous in cases where low signal-to-noise ratio make a correct measurement of the field difficult. Jezzard and Balaban fitted a 2-D polynomial surface to the field map and Hutton et al. used a linear combination (the 8 lowest frequency components) of the discrete cosine set of transformations. Although this approach allows modelling of the field in regions with low SNR, it is vulnerable in regions of the brain where the field varies rapidly and can

introduce blurring artefacts. This applies also to the case of smoothing with e.g. a large Gaussian kernel (with a large FWHM). A problem with the field map method is the assignment of correct image intensity to a shifted voxel. If the distortion has caused voxels to overlap, the field map does not contain any information on how the voxel intensities shall be distributed in the corrected image. Intensity corrections can be made in order to minimize this problem, but has the disadvantage of increasing noise in the corrected images if the voxel shift map itself is noisy. There are also differences between using EPI sequences or gradient echo sequences when creating the field maps. A field map based on EPI images has the advantage that it is acquired in a short time as compared to a field map obtained with a gradient echo sequence. This fact also makes the EPI field map less sensitive to artefacts due to patient motion. The EPI field map however suffers from loss of information in regions where magnetic field inhomogeneity are most severe.

The point spread function on the other hand contains information on both the displacement and the intensity of any voxel, and a correction can therefore correctly assign voxel intensities when based on this technique. This is also the case in regions of the brain where the distortion is particularly severe and it is difficult to provide an accurate field map. Furthermore, the PSF is less sensitive to noise than the field map approach and the phase wrapping problem is avoided. The phase unwrapping procedure is also avoided by the techniques proposed by Schmithorst et al. and by Chen and Wyrwicz. The different types of multi-echo reference scans that are proposed in these two works also has the advantage that they encode EPI distortion resulting not only from  $B_0$  inhomogeneities, but also from eddy current effects and chemical shift.

Another advantage of the PSF approach is the possibility to determine the PSF at a higher spatial resolution than the EPI images to be corrected, which further improves the precision of the correction. If field maps are obtained using EPI, this cannot be done without introducing additional distortions in the field maps. The PSF method however is computationally more intensive than the field map method, and requires additional scanning if information on distortion in more than one direction is needed. Since the geometric distortion in EPI images mainly occurs in the phase encoding direction, this is usually not a problem in practice.

The necessity of correction for field inhomogeneities when using EPI can also be expected to diminish with the implementation and development of different scanning techniques such as sensitivity encoded (SENSE) echo planar imaging. This technique utilises the fact that with a receiver placed near the object, the received signal varies with its relative position of origin. This means that information can be obtained from multiple receivers, which implies the possibility of reducing acquisition times, and therefore also the geometric distortion [17]. Other proposed methods uses image reconstruction based on the acquisition of only half of k-space in order to reduce scan times [18].

In conclusion, a tool for assessment and possibly correction of distortion due to magnetic field homogeneity was developed. It was found that the geometrical distortion when using EPI for fMRI purposes at the 3T head scanner (Siemens Magnetom Allegra) at Lund University Hospital is of low magnitude in sensorimotor cortex and in Broca's area. The evaluation has however also shown that there are regions in the brain where the distortion can be quite severe. This supports co-registration of EPI images and anatomical images for the studied regions of activation, but also emphasises the importance of assessing errors due to distortion in other regions. The correction algorithm used in this work shows overall good results but suffers, in addition to the complexity of phase unwrapping, from some drawbacks such as sensitivity to noise and incapability of correction in regions of severe inhomogeneity. For improved correction other techniques could be used, such as the point spread function

approach or the multi-echo reference scan technique. With different image acquisitions techniques, such as segmented EPI or parallel imaging (SENSE), geometrical distortion can be abundantly reduced.

## 6 References

1. Bandettini P A, Wong E C, Hinks R S, Tikofsky R S, Hyde J S, Time Course EPI of Human Brain Function during Task Activation. *Magn. Reson. Med.* 25, 390-397 (1992).
2. Ogawa S, Tank D W, Menon R, Ellermann J M, Kim S-G, Merkle H, Ugurbil K, Intrinsic Signal Changes Accompanying Sensory Stimulation: Functional Brain Mapping with Magnetic Resonance Imaging. *Proc. Natl. Acad. Sci. USA.* 89, 5951-5955 (1992).
3. Kwong K K, Belliveau J W, Chesler D A, Goldberg I E, Weisskoff R M, Poncelett B P, Kennedy D N, Hoppel B E, Cohen M S, Turner R, Cheng H-M, Brady T J, Rosen B R, Dynamic Magnetic Resonance Imaging of Human Brain Activity During Primary Sensory Stimulation. *Proc. Natl. Acad. Sci. USA.* 89, 5675-5679 (1992).
4. Menon R S, Ogawa S, Hu X, Strupp J S, Andersen P, Ugurbil K, Bold Based Functional MRI at 4 Tesla Includes a Capillary Bed Contribution: Echo-Planar Imaging Mirrors Previous Optical Using Intrinsic Signals. *Magn. Reson. Med.* 33, 453-459 (1995).
5. Buxton R B, Wong E C, Frank L R, Dynamics of Blood Flow and Oxygenation Changes During Brain Activation: the Balloon Model. *Magn. Reson. Med.* 39, 855-864 (1998).
6. Jezzard P, Balaban R S, Correction for Geometric Distortion in Echo Planar Images from  $B_0$  Field Variations. *Magn. Reson. Med.* 34, 65-73 (1995).
7. Hutton C, Bork A, Josephs O, Deichmann R, Ashburner J, Turner R, Image Distortion Correction in fMRI: A Quantitative Evaluation. *NeuroImage.* 16, 217-240 (2002)
8. Schmithorst V J, Dardzinski B J, Holland S K, Simultaneous Correction of Ghost and Geometric Distortion Artefacts in EPI Using a Multiecho Reference Scan. *IEEE Transactions on Medical Imaging.* Vol. 20, No. 6, (June 2001).
9. Reber P J, Wong E C, Buxton R B, Frank L R, Correction of Off Resonance-Related Distortion in Echo Planar Imaging Using EPI-Based Field Maps. *Magn. Reson. Med.* 39, 328-330 (1998).
10. Akel J A, Rosenblitt M, Irarrazaval P, Off-resonance correction using an estimated linear time map. *Magn. Reson. Imaging.* 20, 189-198 (2002).
11. Robson M D, Gore J C, Constable R T, Measurement of the Point Spread Function in MRI Using Constant Time Imaging. *Magn. Reson. Med.* 38, 733-740 (1997).
12. Zeng H, Constable R T, Image Distortion Correction in EPI: Comparison of Field Mapping With Point Spread Function Mapping. *Magn. Reson. Med.* 48, 137-146 (2002).
13. Chen N, Wyrwicz A M, Correction for EPI Distortions Using Multi-Echo Gradient-Echo Imaging. *Magn. Reson. Med.* 41, 1206-1213 (1999).
14. Kadah Y M, Hu X, Simulated Phase Rewinding (SPHERE): A Technique for Reducing  $B_0$  Inhomogeneity Effects in MR Images. *Magn. Reson. Med.* 38, 615-627 (1997).
15. Luk-Pat G T, Nishimura D G, Reducing Off-Resonance Distortion by Echo-Time Interpolation. *Magn. Reson. Med.* 45, 269-276 (2001).
16. Jenkinson M, Fast, Automated, N-Dimensional Phase-Unwrapping Algorithm. *Magn. Reson. Med.* 49, 193-197 (2003).
17. Pruessmann K P, Weiger M, Scheidegger M B, Boesiger P, SENSE: Sensitivity Encoding for Fast MRI. *Magn. Reson. Med.* 45, 952-962 (1999).

18. Jesmanowicz A, Bandettini P A, Hyde J S, Single-Shot Half k-Space High-Resolution Gradient-Recalled EPI for fMRI at 3 Tesla. *Magn. Reson. Med.* 40, 754-762 (1998).

# 7 Appendix

## 7.1 The program

```
PRO Distorsion_corr_2

common block,Images,Rec,Phaseimage_wrapped,Shift_map_mm,Slices,Colorbar,done,text,slider
        , $draw1,draw2,draw3,draw4,slice_no
device, decomposed=0

;***** READING FIELD MAPS*****

md = obj_new('mrdta')
ret = md->loadtimesequences( path='m:XXXXXXXXXX\Series 004 gre_field_mapping'
        , $ progressbar=0,errno=errno, errtxt=errtxt )

field_maps = *(md->getdata())
print, 'Number of pictures in the sequence:', md->getNofImages()
print, 'Number of slices in the sequence :', md->getNofSlices()
slices=md->getNofSlices()
Field=fltarr(64,64,slices)
for i=0,slices-1 do begin
        Field(*,*,i)=*(field_maps(0,i))
endfor

;***** READING EPI IMAGES*****

path1 = "m:XXXXXXXXXX\Series 005 ep2d_bold\1.3.12.2.1107.5.2.7.20410.4.0.2166574324302049.dcm"
EPIdata =obj_new('IDLffDicom',path1)

Rowptr = EPIdata -> GetValue('0028'x,'0010'x)
Rows = *Rowptr[0]
OBJ_DESTROY, EPIdata
Image1=read_dicom("m:XXXXXXXXXX\Series 005
ep2d_bold\1.3.12.2.1107.5.2.7.20410.4.0.2166574324302049.dcm")
Matsize=64

NofEPI_indexes=Rows/64.0
NofEPI_images=NofEPI_indexes^2

Images=fltarr(Matsize,Matsize,slices); Ändrat NofEPI_images till slices
slice_no=0

for i=0,NofEPI_indexes-1 do begin
        for j=0,NofEPI_indexes-1 do begin
                if slice_no lt slices then begin
                        Images(*,*,slice_no)=Image1(64*j:64*(j+1)-1,64*i:64*(i+1)-1)
                        slice_no=slice_no+1
                endif
        endfor
endfor
print,size(images)
```



```

***** FIELD MAP DATA *****
,
TE1=4.89*(10.0)^(-3)
TE2=7.35*(10.0)^(-3)
deltaTE=TE2-TE1
gyro=42.6*(10.0)^6
T_acq=28.2 *(10.0)^(-3)
scale=4096/(2.0*PI)

. *****
,
image2=(Field/scale)
phaseimage_wrapped=image2-!PI
phaseimage=phaseimage_wrapped

;phaseimage=smooth(phaseimage,3, /edge_truncate)

. ***** UNWRAPPING *****
,
for d=0,slices-1 do begin

    B=phaseimage(*,*,d)
    limit=0.1*max(Images(*,*,d))
    Mask=Bytarr(Matsize,Matsize)
    Mask(where(Images(*,*,d) gt limit))=1
    Partition=Bytarr(Matsize,Matsize)

***** NO. OF INTERVALS*****
,

Nof_intervals=4
interv=(2.0*PI)/Nof_intervals
for i=1,Nof_intervals do begin
    Partition(where((B ge (-!PI+(i-1)*interv)) and (B lt (-!PI+i*interv))))=i
endfor

Partition=Partition*Mask

***** CREATING ORIGINAL REGIONS*****
,

Regions=Bytarr(Matsize,Matsize)
Temp=Bytarr(Matsize,Matsize)
n=0
reg_no=0
pos=0

while (n lt Matsize*Matsize) do begin
    row=fix(float(pos)/Matsize)
    col=float(pos)-row*Matsize
    if (Temp(col,row) ne 1) then begin
        s=search2d(Partition,col,row,Partition(col,row),Partition(col,row),/diagonal)
        Regions(s)=reg_no
        n=n+n_elements(s)
        reg_no=reg_no+1
        Temp(s)=1
    endif
    pos=pos+1
endwhile

print,"Antal reg:",reg_no
Remain=reg_no

```

```

while Remain gt 1 do begin

    Temp=Temp*0
    Diff=fltarr(reg_no,reg_no)
    Nof_interf=fltarr(reg_no,reg_no)

    for i=1,Matsize-2 do begin
        for j=1,Matsize-2 do begin

            if (Temp(i+1,j) ne 1) then begin
                if (Regions(i,j) ne Regions(i+1,j)) then begin

Diff(Regions(i,j),Regions(i+1,j))=Diff(Regions(i,j),Regions(i+1,j))+(B(i,j)-B(i+1,j))
Nof_interf(Regions(i,j),Regions(i+1,j))=Nof_interf(Regions(i,j),Regions(i+1,j))+1

                endif

            endif

            if (Temp(i-1,j) ne 1) then begin
                if (Regions(i,j) ne Regions(i-1,j)) then begin

Diff(Regions(i,j),Regions(i-1,j))=Diff(Regions(i,j),Regions(i-1,j))+(B(i,j)-B(i-1,j))
Nof_interf(Regions(i,j),Regions(i-1,j))=Nof_interf(Regions(i,j),Regions(i-1,j))+1

                endif

            endif

            if (Temp(i,j+1) ne 1) then begin
                if (Regions(i,j) ne Regions(i,j+1)) then begin

Diff(Regions(i,j),Regions(i,j+1))=Diff(Regions(i,j),Regions(i,j+1))+(B(i,j)-B(i,j+1))
Nof_interf(Regions(i,j),Regions(i,j+1))=Nof_interf(Regions(i,j),Regions(i,j+1))+1

                endif

            endif

            if (Temp(i,j-1) ne 1) then begin
                if (Regions(i,j) ne Regions(i,j-1)) then begin

Diff(Regions(i,j),Regions(i,j-1))=Diff(Regions(i,j),Regions(i,j-1))+(B(i,j)-B(i,j-1))
Nof_interf(Regions(i,j),Regions(i,j-1))=Nof_interf(Regions(i,j),Regions(i,j-1))+1

                endif

            endif

            if (Temp(i+1,j+1) ne 1) then begin
                if (Regions(i,j) ne Regions(i+1,j+1)) then begin

Diff(Regions(i,j),Regions(i+1,j+1))=Diff(Regions(i,j),Regions(i+1,j+1))+(B(i,j)-B(i+1,j+1))
Nof_interf(Regions(i,j),Regions(i+1,j+1))=Nof_interf(Regions(i,j),Regions(i+1,j+1))+1

                endif

            endif

            if (Temp(i-1,j+1) ne 1) then begin
                if (Regions(i,j) ne Regions(i-1,j+1)) then begin

Diff(Regions(i,j),Regions(i-1,j+1))=Diff(Regions(i,j),Regions(i-1,j+1))+(B(i,j)-B(i-1,j+1))
Nof_interf(Regions(i,j),Regions(i-1,j+1))=Nof_interf(Regions(i,j),Regions(i-1,j+1))+1

                endif

            endif

        endfor
    endfor
endwhile

```

```

                                endif
                            endif

                            if (Temp(i+1,j-1) ne 1) then begin
                                if (Regions(i,j) ne Regions(i+1,j-1)) then begin

Diff(Regions(i,j),Regions(i+1,j-1))=Diff(Regions(i,j),Regions(i+1,j-1))+(B(i,j)-B(i+1,j-1))
Nof_interf(Regions(i,j),Regions(i+1,j-1))=Nof_interf(Regions(i,j),Regions(i+1,j-1))+1

                                endif
                            endif

                            if (Temp(i-1,j-1) ne 1) then begin
                                if (Regions(i,j) ne Regions(i-1,j-1)) then begin

Diff(Regions(i,j),Regions(i-1,j-1))=Diff(Regions(i,j),Regions(i-1,j-1))+(B(i,j)-B(i-1,j-1))
Nof_interf(Regions(i,j),Regions(i-1,j-1))=Nof_interf(Regions(i,j),Regions(i-1,j-1))+1

                                endif
                            endif

                            Temp(i,j)=1

                            endfor
                        endfor

                    Temp1=bytarr(reg_no,reg_no)
                    for i=0,reg_no-1 do begin
                        for j=0,reg_no-1 do begin
                            if (Temp1(i,j) ne 1) then begin
                                Diff(i,j)=Diff(i,j)-Diff(j,i)
                                Diff(j,i)=0
                                Nof_interf(i,j)=Nof_interf(i,j)+Nof_interf(j,i)
                                Nof_interf(j,i)=0
                                Temp1(j,i)=1
                            endif
                        endfor
                    endfor

                    K=fltarr(reg_no,reg_no)
                    L=fltarr(reg_no,reg_no)

                    K(where(Nof_interf ne 0))=(-Diff(where(Nof_interf ne 0)))/(2.0*!PI*
$Nof_interf(where(Nof_interf ne 0)))
                    L=round(K)
                    Diff_KL=abs(K-L)
                    Tot=Nof_interf*(0.5-Diff_KL)
                    merge_pos=where(tot eq max(tot))
                    merge_row=fix(float(merge_pos(0))/reg_no)
                    merge_col=fix(float(merge_pos(0))-merge_row*reg_no)

                    B(where(Regions eq merge_row))=B(where(Regions eq merge_row))-
$2.0*!PI*L(merge_col,merge_row)
                    Regions(where(Regions eq merge_row))=merge_col
                    Remain_reg=merge_col
                    Remain=n_elements(Regions[uniq(Regions, sort(Regions))])
                    print,"Slice no:",d+1," Regions remaining:",Remain,L(merge_col,merge_row)

                endwhile

```

```

        phaseimage(*,*,d)=B
    endfor

;*****
;

matsize=64
Images=rebin(images,Matsize,Matsize,slices)

; ***** CREATING PIXEL SHIFT MAP*****

phaseimage=rebin(phaseimage,matsize,matsize,slices)
deltaB=((2.0*!PI*gyro*deltaTE)^(-1))*phaseimage
shift_map=gyro*deltaB*T_acq
shift_map_mm=shift_map*3.0

; ***** CORRECTION*****
Rec=fltarr(matsize,matsize,slices)

for k=0,slices-1 do begin
    for i=0,matsize-1 do begin
        for j=0,matsize-1 do begin
            pos=j+(shift_map(i,j,k))*(matsize/64.0)
            if pos gt 0 then begin
                Rec(i,j,k)=interpolate(Images(i,*,k),pos,$
                    cubic=-0.5,missing=0) > 0
            endif
        endfor
    endfor
endfor

colorbar=replicate(1b,20)#bindgen(256)

end
;*****

PRO make_image,b1=im1,b2=im2,b3=im_der
common block

Im1=indgen(64,64,2)
Im2=indgen(64,64)
Im2(*,32)=0
Im2(32,*)=0
Im_der=sobel(Im1(*,*,0))
Im1_1=Im1(*,*,0)
Im1(30:50,30:50,0)=0

end

;*****
;

```

```

PRO Dist_corr_eval_2_event, ev
common block

widget_control, ev.id, get_uvalue = uv; /draw_button_events
if (n_elements(uv) eq 0) then uv=""; return

name = strmid(tag_names(ev, /structure_name), 7, 4)

if (uv eq 'DONE') then widget_control, ev.top, /draw_button_events, /destroy
    if (uv eq "SLID") then begin

        slice_no=ev.value
        print,slice_no
        widget_control, get_value=window, draw1
        wset,window
        tvscl, rebin(rotate(Phaseimage_wrapped(*,*,ev.value),2),256,256),0,0
        widget_control, get_value=window, draw2
        wset,window
        plot,[min(shift_map_mm(*,*,ev.value)),max(shift_map_mm(*,*,ev.value))],yrange=[min
        $(shift_map_mm(*,*,ev.value)),max(shift_map_mm(*,*,ev.value))],/nodata,color=255,
        $position=[30/326.0,10/276.0,50/326.0,266/276.0],
        $xticks=1,xstyle=1,ystyle=1,xtickformat='(A1)'
        tv, bytscl(colorbar),30,10
        tvscl, rebin(rotate(shift_map_mm(*,*,ev.value),2),256,256),60,10; ax=20, az=10
        widget_control, get_value=window, draw3
        wset,window
        tvscl, rebin(rotate(Images(*,*,ev.value),2),256,256);,256,0
        widget_control, get_value=window, draw4
        wset,window
        tvscl, rebin(rotate(Rec(*,*,ev.value),2),256,256);,256,0

    endif

endif

if (name eq "DRAW") then begin

    if (ev.press eq 1) then begin
        print, ev.x, ev.y
        x=ev.x
        y=ev.y
        roisize=20
        widget_control, get_value=window, draw3
        wset,window
        plots,x,y,/device
        plots,x+roisize+1,y,/continue,/device
        plots,x+roisize+1,y+roisize+1,/continue,/device
        plots,x,y+roisize+1,/continue,/device
        plots,x,y,/continue,/device
        widget_control, get_value=window, draw2
        wset,window
        xx=x+60
        yy=y+10
        plots,xx,yy,/device
        plots,xx+roisize+1,yy,/continue,/device
        plots,xx+roisize+1,yy+roisize+1,/continue,/device
        plots,xx,yy+roisize+1,/continue,/device
        plots,xx,yy,/continue,/device
        shift_map_mm_1=rotate(shift_map_mm(*,*,slice_no),2)
        ;shift_map_mm_1=rotate(rebin(shift_map_mm(*,*,slice_no),256,256),2)
        x=fix(x/4.0)
    endif
endif

```

```

y=fix(y/4.0)

result1 = string(format="(' Max:', F6.2, ")",
$max(shift_map_mm_1(x+1:x+10,y+1:y+10)))
result2 = string(format="(' Min:', F6.2, ")",
$min(shift_map_mm_1(x+1:x+10,y+1:y+10)))
result3 = string(format="(' Mean:', F6.2, ")",
$mean(shift_map_mm_1(x+1:x+10,y+1:y+10)))
result4 = string(format="(' Stddev:', F6.2, ")",
$stddev(shift_map_mm_1(x+1:x+10,y+1:y+10)))
widget_control, text , set_value=result1
widget_control, text , set_value=result2,/append
widget_control, text , set_value=result3,/append
widget_control, text , set_value=result4,/append

endif

if (ev.press eq 4) then begin
    widget_control, get_value=window, draw2
    wset,window
    tvscl,rebins(rotate(shift_map_mm(*,*,slice_no),2),256,256),60,10
    widget_control, get_value=window, draw3
    wset,window
    tvscl,rebins(rotate(Images(*,*,slice_no),2),256,256)
endif

endif
end
*****

PRO Dist_corr_eval_2
common block

loadct,0
base = widget_base(title='Interface', xsize=670, ysize=552)
Distorsion_corr_2

done = widget_button(base, value = 'Done', uvalue = 'DONE',xoffset=606, xsize=40,yoffset=20, ysize=35)
text = widget_text(base,xoffset=590, xsize=11,yoffset=135, ysize=4)
slider = widget_slider(base,maximum=slices-1, uvalue = "SLID",title='Slice no.',xoffset=590,
xsize=72,yoffset=110,$ ysize=10)
draw1 = widget_draw(base,xoffset=0, xsize=256,yoffset=0, ysize=276, /button_events);/motion_events)
draw2 = widget_draw(base,xoffset=256,xsize=326, yoffset=0,ysize=276, /button_events);/motion_events)
draw3 = widget_draw(base,xoffset=0,xsize=256,yoffset=276, ysize=276, /button_events);/motion_events)
draw4 = widget_draw(base,xoffset=256,xsize=326,yoffset=276, ysize=276, /button_events);/motion_events)
label = widget_label(value="Results (mm)",base,xoffset=590,yoffset=195)
slice_no=0

widget_control, base, /realize
widget_control, get_value=window,draw1
wset,window
tvscl,rebins(rotate(Phaseimage_wrapped(*,*,0),2),256,256),0,0

widget_control, get_value=window, draw2
wset,window
tv,bytscl(colorbar),30,10
tvscl,rebins(rotate(shift_map_mm(*,*,0),2),256,256),60,10;ax=20,az=10
plot,[min(shift_map_mm(*,*,0)),max(shift_map_mm(*,*,0))],yrange=[min(shift_map_mm(*,*,0)),
$max(shift_map_mm(*,*,0))],$/nodata,color=255,position=[30/326.0,10/276.0,50/326.0,266/276.0],xticks=1,
$/noerase,xstyle=1,ystyle=1,xtickformat='(A1)'

```

```
widget_control, get_value=window, draw3
wset,window
tvsc1,rebin(rotate(Images(*,*,0),2),256,256);,256,0
```

```
widget_control, get_value=window, draw4
wset,window
tvsc1,rebin(rotate(Rec(*,*,0),2),256,256);,256,0
```

```
xmanager, 'Dist_corr_eval_2', base, /no_block
```

```
end
```

```
*****
```